Mainz Microtron MAMI

A1 Collaboration

Spokesperson: H. Merkel

Letter of Intent

Measurement of the Electromagnetic Transition Form Factor of the π^0 in the space-like region via Primakoff Electroproduction

L. Capozza[1,2], M. Gorshteyn[1,2], F. Maas[1,2], O. Noll[1,2], S. Wolff[1,2]

[1]Institut für Kernphysik, Johannes Gutenberg-Universität Mainz
[2]Helmholtz-Institut Mainz, GSI Helmholtzzentrum für Schwerionenforschung GmbH

Contact persons:

L. Capozza (lcapozza@uni-mainz.de)
F. Maas (maas@uni-mainz.de)

Abstract

We propose a determination of the pion transition form factor (TFF) $F_{\pi^0\gamma^*\gamma^*}$ with two spacelike virtual photons in the region of low Q^2 by a measurement of the π^0 electroproduction cross section in the Primakoff kinematical regime. Exclusive electroproduction events need to be identified, where both the scattered electron and the produced pion are detected in the forward scattering region in coincidence. We propose to perform this experiment at the A1 facility at MAMI, by upgrading the available setup with an electromagnetic calorimeter which is originally designed for the PANDA experiment at FAIR, within the framework of the so-called "phase 0" of the FAIR project. Measurements of the cross section with statistical uncertainties at the percent level for several Q2 values up to 0.06 GeV^2 and 0.01 GeV^2 for the two virtualities, respectively, are feasible within measuring times of 1000 hours or less. At present, only single-virtual TFF data, coming from π^0 production in e^+e^- collisions, are available in the spacelike region, at the lowest Q^2 of 0.3 GeV^2. TFF data with two virtual photons, with emphasis on the low-Q^2 regime, are needed to provide a more precise estimate of the so-called hadronic light-by-light scattering contribution to the anomalous magnetic moment of the muon a_μ. An important uncertainty in the Standard Model prediction for a_μ comes from this contribution.

1 Physics Motivation

The anomalous magnetic moment of the muon $a_\mu = (g-2)_\mu/2$, the deviation of the muon gyromagnetic ratio g from the value for a point-like spin-1/2 Dirac particle, $g = 2$, arises due to the Standard Model radiative corrections. The comparison of very accurate theoretical calculations with an equally precise measurement of a_μ offers a very sensitive test of the Standard Model in the electroweak and strong sectors.

Currently, a 4σ discrepancy of the SM theory [1, 2]

$$a_\mu^{SM} = 116\,591\,828\,(50) \times 10^{-11} \tag{1}$$

with the measurement at BNL is observed [3],

$$a_\mu^{exp} = 116\,592\,089\,(63) \times 10^{-11} \tag{2}$$

A new, more precise measurement at Fermilab is ongoing [4], aiming to reduce the experimental error by a factor of 4. Should the deviation from the SM prediction persist, it would hint to particles or interactions beyond the Standard Model.

As experimental effort is being undertaken, aiming at reducing the experimental uncertainties, also the theoretical prediction needs to be constrained with higher accuracy. To that end, a full set of QED corrections at five-loop accuracy [5],

$$a_\mu^{QED} = 116\,584\,718.951\,(80) \times 10^{-11}, \tag{3}$$

and electroweak corrections at two-loop accuracy [6]

$$a_\mu^{EW} = 153.6\,(1.0) \times 10^{-11}, \tag{4}$$

have been reliably calculated. The uncertainty of these contributions does not pose any limitation to the interpretation of the experimental results.

Whenever the strong interaction is involved, the same level of accuracy as for QED and weak corrections can not be achieved. The two relevant hadronic contributions to a_μ are the hadronic vacuum polarisation (HVP) which arises at two-loop (Fig. 1 (a)) and three-loop level (Fig. 1 (b-d)) (order $O(\alpha^2)$ and $O(\alpha^3)$, respectively), and the hadronic light-by-light (HLbL) scattering (Fig. 1 (e)) arising at three-loop ($O(\alpha^3)$).

Recent improvement in the theory error estimates for the hadronic contributions to a_μ rely on a data-driven approach. For instance, the leading-order HVP contribution is expressed as

$$a_\mu^{HVP\,LO} = \left(\frac{\alpha m_\mu}{3\pi}\right)^2 \int_{4m_\pi^2}^{\infty} \frac{ds}{s^2} K(s) R(s), \quad \text{where} \quad R = \frac{\sigma_{tot}(e^+e^- \to \text{hadrons})}{\sigma(e^+e^- \to \mu^+\mu^-)}, \tag{5}$$

which directly uses the measured cross sections for $e^+e^- \to$ hadrons as input, and $K(s)$ a known kinematical factor. Moreover, the $1/s^2$ weighting with energy results in an enhanced sensitivity to the lower part of the hadronic spectrum, which is well known experimentally. The most recent evaluation of the HVP contribution leads to [2]

$$a_\mu^{HVP(2+3-loop)} = 6\,851\,(43) \times 10^{-11}. \tag{6}$$

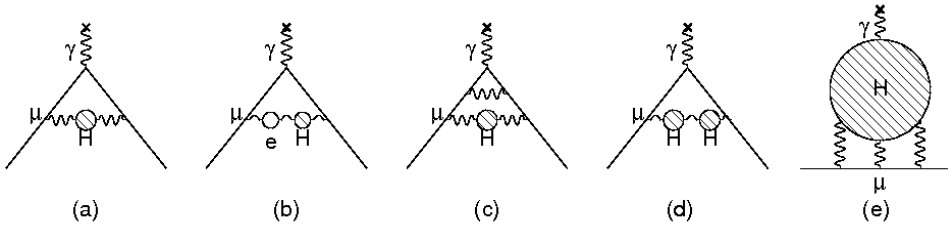

Figure 1: Hadronic contributions to the muon anomaly: HVP two-loop (diagram a), HVP three-loop (diagrams b-d), and HLbL (diagram e)

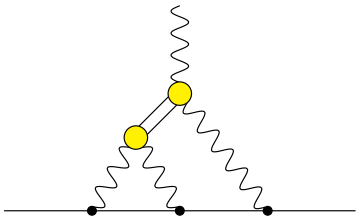

Figure 2: Pseudoscalar meson pole contribution to a_μ. The double line represents the propagators of π^0, η and η' mesons. The associated permutations of this diagram are not shown.

The HLbL contribution, according to "Glasgow Consensus" [7], amounts to

$$a_\mu^{HLbL} = 105\,(26) \times 10^{-11}. \tag{7}$$

Although HLbL is suppressed by one power of α with respect to HVP, the uncertainties are of the same order.

This relatively large uncertainty is due to the fact that it is in general impossible to represent the HLbL contribution to a_μ as an integral over the data, in the spirit of Eq. 5. Recently, dispersion theory was applied to the HLbL amplitude [8, 9, 10], allowing to relate this contribution to quantities measurable in the $\gamma^*\gamma^*$-fusion process. Similarly to the case of HVP, the integral is strongly weighted towards the lower part of the spectrum of $\gamma^*\gamma^* \to$ hadrons, and the dominant contribution to a_μ^{HLbL} comes from light pseudoscalar mesons propagating between the two-photon vertices, as depicted in Fig. 2. Its contribution to the muon anomaly is given by an integral over the meson transition form factor $F_{PS\gamma^*\gamma^*}(Q_1^2, Q_2^2)$, which is a function of the (spacelike) photon virtualities $Q_{1,2}^2$ according to

$$a_\mu^{HLbL,\,PS} = \int_0^\infty dQ_1 \int_0^\infty dQ_2 \int_{-1}^{1} d\tau\; w(Q_1, Q_2, \tau) F_{PS\gamma^*\gamma^*}(-Q_1^2, -(Q_1{+}Q_2)^2) F_{PS\gamma^*\gamma^*}(-Q_2^2, 0), \tag{8}$$

with $PS = \pi^0, \eta, \eta'$, and a known kinematical weighting function w. The evaluation of the above integral signals a significant model dependence as the results range from

$57(4)\times10^{-11}$ for the π^0 contribution and $83(6)\times10^{-11}$ for $\pi^0+\eta+\eta'$ in the vector meson dominance (VMD) model [11], to $77(7)\times10^{-11}$ and $114(10)\times10^{-11}$ in a VMD model with explicit operator product expansion constraints [12]. Data driven approaches that use rational approximants to parametrise the pseudoscalar form factors obtain values between the two extremes, $63.6(2.7)\times10^{-11}$ and $94.3(5.3)\times10^{-11}$, respectively [13].

The value of the form factor in the real photon limit with respect to both virtualities is on the one hand given by the chiral anomaly, $F_{\pi^0\gamma\gamma}(0,0) = (4\pi^2 F_\pi)^{-1}$, with $F_\pi = 92.4$ MeV the pion decay constant. On the other hand, it is related to the π^0 radiative decay width, according to

$$\Gamma_{\gamma\gamma} = \frac{1}{4}\pi\alpha^2 m_\pi^3 |F_{\pi^0\gamma\gamma}(0,0)|^2, \tag{9}$$

with $\Gamma_{\gamma\gamma} = 7.82(14)(17)$ eV obtained by the PRIMEX collaboration [14]. The two ways to obtain the normalisation are in excellent agreement with each other (including small chiral corrections to the anomaly [15]).

The analysis of the body of data from CELLO, CLEO, BABAR and Belle with one spacelike photon with Padé approximants [13] results in a very precise low-Q^2 parametrisation of the Q^2-dependence of the pion form factor,

$$\frac{F_{pi^0\gamma^*\gamma}(-Q^2,0)}{F_{pi^0\gamma^*\gamma}(0,0)} = 1 - a_\pi \frac{Q^2}{m_\pi^2} + b_\pi \left(\frac{Q^2}{m_\pi^2}\right)^2, \tag{10}$$

with the slope and curvature parameters $a_\pi = 0.0324(12)(19)$ and $b_\pi = 0.00106(09)(25)$, respectively. The first and the second number in the parentheses denote the statistical and systematical uncertainty, respectively.

The aim of the experiment proposed in this letter of intent is to improve the precision both of the measurement of the π^0 decay width, and of the form factor. We will study the doubly-virtual case at very low spacelike virtualities $q_{1,2}^2 = -Q_{1,2}^2 < 0$, for which

$$\frac{F_{pi^0\gamma^*\gamma\gamma^*}(-Q_1^2,-Q_2^2)}{F_{pi^0\gamma^*\gamma^*}(0,0)} = 1 - a_\pi \frac{Q_1^2+Q_2^2}{m_\pi^2} + b_\pi \frac{Q_1^4+Q_2^4}{m_\pi^4}. \tag{11}$$

2 Pion TFF via Primakoff effect

The Primakoff effect [16] is the production of a π^0 by a high-energy real photon in the Coulomb field of a nucleus A, consisting of Z protons and N neutrons, via the process $\gamma + A(Z,N) \to \pi^0 + A(Z,N)$. This experimental method has recently been used by the PRIMEX collaboration [14] to obtain the to date most precise measurement of the π^0 two-photon width, $\Gamma_{\gamma\gamma} = 7.82(14)(17)$ eV.

To go beyond the real photon point and address the π^0 transition form factor, π^0 coherent electroproduction should be studied,

$$e + A(Z,N) \to e + A(Z,N) + \pi^0 \tag{12}$$

The four momenta of incoming and outgoing electron are denoted as $k = (E, \mathbf{k})$ and $k' = (E', \mathbf{k}')$, respectively, and the four momentum transfer from the electron is

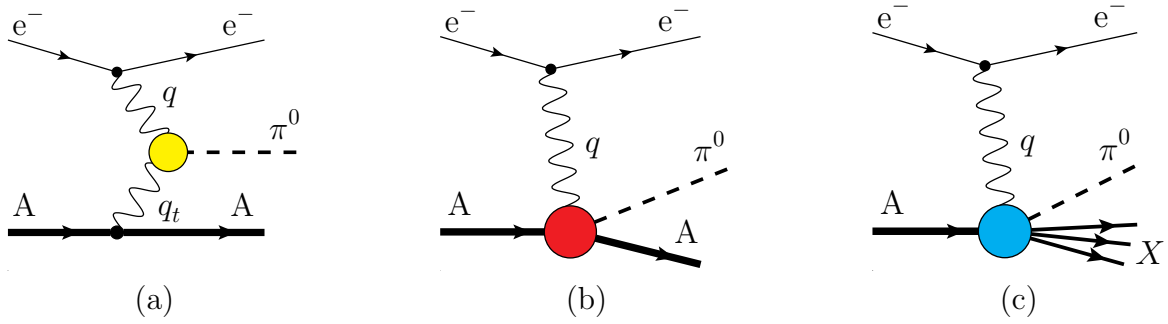

Figure 3: Contributions to the π^0 electroproduction on a nucleus: Primakoff (a), strong coherent (b) and incoherent (c) mechanisms. The X in the final state of diagram (c) indicates any break-up state of the nucleus, where the single nucleon knock-out, $X = (A-1)+p,n$, is the predominant one.

$q = k - k'$ as $q = (\nu, \mathbf{q})$. The pion four momentum is $k_\pi = (\omega_\pi, \mathbf{k}_\pi)$ and m_π the π^0 mass. Finally, the four-momentum transfer to the nucleus is $q_t = q - k_\pi$. Both transferred four-momenta are spacelike, $q^2 = -Q^2 < 0$ and ${q_t}^2 = t < 0$.

Generally, there are three distinct contributions to the π^0 production on a nucleus: along with the mechanism of interest, the Primakoff effect (diagram (a) in Fig. 2), strong coherent production (diagram (b) in Fig. 2) and incoherent (diagram (c) in Fig. 2) mechanisms contribute.

The scattering amplitude underlying the Primakoff mechanism is given by

$$T_{Prim} = 2M_A \frac{e^3 Z}{t} F_{Ch}(t) F_{\pi^0\gamma^*\gamma^*}(-Q^2, t) \epsilon^\mu(q)\, \varepsilon_{0\alpha\beta\mu} q^\alpha k_\pi^\beta, \tag{13}$$

where the laboratory frame with the target nucleus at rest was used, $P^\mu = (M_A, \vec{0})$, with P the nucleus four-momentum and M_A its mass. Furthermore, $\epsilon^\mu(q)$ stands for the virtual photon polarisation vector, and the sign of the totally antisymmetric tensor is fixed according to $\varepsilon_{0123} = +1$. The pion TFF explicitly enters the amplitude along with $F_{Ch}(t)$, which denotes the nuclear charge form factor. The latter is related to the nuclear charge density ρ_{Ch} and known from elastic electron scattering [17]. The four-fold differential cross section reads

$$\frac{d^4\sigma}{dQ^2 d\nu d\Omega_\pi} = \frac{\alpha}{\pi} \frac{|\mathbf{q}|}{2E^2 Q^2 (1-\epsilon)} \frac{d\sigma}{d\Omega_\pi}, \tag{14}$$

with the virtual photon cross section given by

$$\frac{d\sigma}{d\Omega_\pi} = 8\alpha Z^2 \Gamma_{\gamma\gamma} \frac{\nu^3 |\mathbf{q}| \beta_\pi^3}{m_\pi^3 t^2} |F_{Ch}(t)|^2 \left| \frac{F_{pi^0\gamma^*\gamma\gamma^*}(-Q^2, t)}{F_{pi^0\gamma^*\gamma^*}(0,0)} \right|^2 \sin^2\theta_\pi (1 - \epsilon \cos 2\phi), \tag{15}$$

with ϵ the usual virtual photon polarisation parameter, $\beta_\pi = \sqrt{1 - m_\pi^2/\nu^2}$, θ_π the angle between the pion and the virtual photon momenta, and ϕ the angle between

the electron scattering plane and the outgoing pion. From Eq. 15 it is seen that a measurement of the Primakoff cross section gives a direct access to both the $\pi^0 \to \gamma\gamma$ decay width, and to the TFF. To disentangle the two, measurements at several values of Q^2 are necessary.

The amplitude for the strong coherent production at high energies proceeds predominantly via the exchange of an ω meson [18, 19], which for $|t| \ll m_\omega^2$, with $m_\omega = 782.65(12)$ MeV the ω meson mass, reads

$$T_{Coh} = 2M_A \frac{e}{-m_\omega^2} F_{St}(t) F_{\pi^0\omega\gamma^*}(-Q^2, t) \epsilon^\mu(q)\, \varepsilon_{0\alpha\beta\mu} q^\alpha k_\pi^\beta, \tag{16}$$

with the strong nuclear form factor related to the nuclear density ρ_A which is assumed to follow the charge density but is normalised to the atomic weight A, rather than charge Z, $\rho_A = (A/Z)\rho_{Ch}$. Moreover, for a qualitative understanding we notice here that nuclear saturation [21] leads to the ω meson effectively interacting only with the nucleons on the surface of the nucleus, rather than the whole volume, changing the scaling from A to $A^{2/3}$. It is thus useful to report here the naive VMD model expectation for the ratio of the strong coherent and the Primakoff amplitudes,

$$|T_{Coh}^{VMD}/T_{Prim}| \sim \frac{A^{2/3}}{Z} \frac{g_\omega^2}{16\pi\alpha} \frac{|t|}{m_\omega^2}, \tag{17}$$

with $g_\omega = 17.1$ the $\gamma - \omega$ coupling determined from the electronic width of the ω meson [20]. Then, the total coherent cross section reads

$$\frac{d\sigma}{d\Omega_\pi} \approx \frac{d\sigma^{\text{Primakoff}}}{d\Omega_\pi} \left| 1 + e^{i\phi} \frac{A^{2/3}}{Z} \frac{g_\omega^2}{16\pi\alpha} \frac{|t|}{m_\omega^2} \right|^2, \tag{18}$$

with the purely Primakoff cross section given by Eq. (15) and the relative phase $\phi \approx 0.88$ [19]. Plugging in numbers, we expect for the case of ^{181}Ta the Primakoff to dominate for $|t| \ll 0.002$ GeV^2.[1] For a realistic calculation that goes beyond the naive VMD expectation of Eq. 17, Glauber (multiple scattering) theory, incorporating effects of absorption and rescattering of pions by the nucleus, shadowing of high-energy virtual photons, and nuclear saturation, is employed [25]. This framework was successfully applied to the analysis of the Primakoff and background processes in the past [18, 19].

Finally, incoherent production is accompanied by the knock-out of one or more nucleons. For the sake of a simple qualitative estimate, one can assume that the ω exchange is the leading mechanism for the incoherent scattering, as well. In that case, the incoherent cross section is simply a sum of equal cross sections on A nucleons. Taking into account nuclear saturation, in high-energy collisions $A \to A_{eff}$, with $A_{eff} \approx 0.6A$, e.g. for lead [21]. Finally, the momentum transfer t is now transferred not to a nuclear state, but to a nucleon. This leads to an expectation

$$\frac{d\sigma}{d\Omega_\pi} \approx \frac{d\sigma^{\text{Primakoff}}}{d\Omega_\pi} \frac{A_{eff}}{Z^2} \left| \frac{g_\omega^2}{16\pi\alpha} \frac{t}{m_\omega^2} \frac{G_E^p(t)}{F_{Ch}(t)} \right|^2, \tag{19}$$

[1] Note that the ρ^0 meson exchange also contributes, but since it couples to the protons and neutrons with the opposite sign, and the respective VMD coupling $g_\rho \sim (1/3)g_\omega$, its overall contribution is expected to contribute only a few percent of the ω-mediate coherent production.

with G_E^p the proton's electric form factor. The model of Ref. [22] goes beyond this simple estimate, including effects of multiple scattering, nuclear absorption and shadowing, and is employed to describe this contribution in a realistic calculation [25].

3 Proposed Experiment

3.1 Kinematics

The single π^0 electroproduction reaction given in eq. (12) has a three-body final state and its kinematics is fully determined by 5 independent variables. Detecting 2 final state particles and measuring their momenta gives 6 constraints, fixing the kinematics exclusively with one redundant quantity. Since the momentum of the recoil nucleus is too small for the particle to reach a detector, both electron and pion need to be detected.

Given that the Primakoff contribution is proportional to Z^2, the choice of a high-Z target is necessary. This implies that the mass of the target will also be large and thus the kinetic energy absorbed by the nucleus can be neglected. Consequently, the beam energy is shared completely by the scattered electron and the pion, i.e. $\nu \simeq \omega_\pi$. The four momentum transfer to the target nucleus is thus given by $q_t \simeq (0, \mathbf{q_t})$, resulting in $t = -\mathbf{q_t}^2$. From the momentum conservation relation $\mathbf{q} = \mathbf{k}_\pi + \mathbf{q_t}$, the following expression for t can be derived:

$$-t = 2\nu^2 + Q^2 - m_\pi^2 - 2\sqrt{\nu^2 + Q^2}\sqrt{\nu^2 - m_\pi^2}\cos\theta_{\pi q} \ , \tag{20}$$

where $\theta_{\pi q}$ is the angle between the pion momentum and the momentum transfer $\mathbf{q}$ in the laboratory frame. From Eq. (20), the kinematical conditions for minimising $|t|$ can be derived.

Firstly, the pion energy ν should be maximised. This happens if the beam energy is large and the scattering electron energy is small. In the following, the maximum beam energy of 1.5 GeV available at MAMI is considered, although slightly lower beam energies of the order of 1.2 GeV might improve the possible acceptance and thus the overall result of the experiment. The optimal beam energy will be subject of further studies and not treated in this letter. As for the scattered electron energy E', the detection and resolution capabilities limit the accessible range from below. As lower limit for E', the value of 100 MeV will be assumed.

Secondly, only measurements at relatively small Q^2 are possible, if the value of $|t|$ has to stay limited. Neglecting the electron mass, the expression $Q^2 = 2EE'(1-\cos\theta_e)$ can be derived, where θ_e is the polar scattering angle of the electron in the laboratory frame. Since the beam energy has to be large and E' is limited from below, the angle θ_e needs to be kept rather small. This means that the momentum transfer $\mathbf{q}$ will also have a small polar angle θ_q.

Thirdly, the angle $\theta_{\pi q}$ should be as small as possible. Values of $\theta_{\pi q}$ within few degrees turn out to be optimal for the sensitivity to the Primakoff contribution. If both θ_q and $\theta_{\pi q}$ are small, then the pion momentum itself will make a small angle with

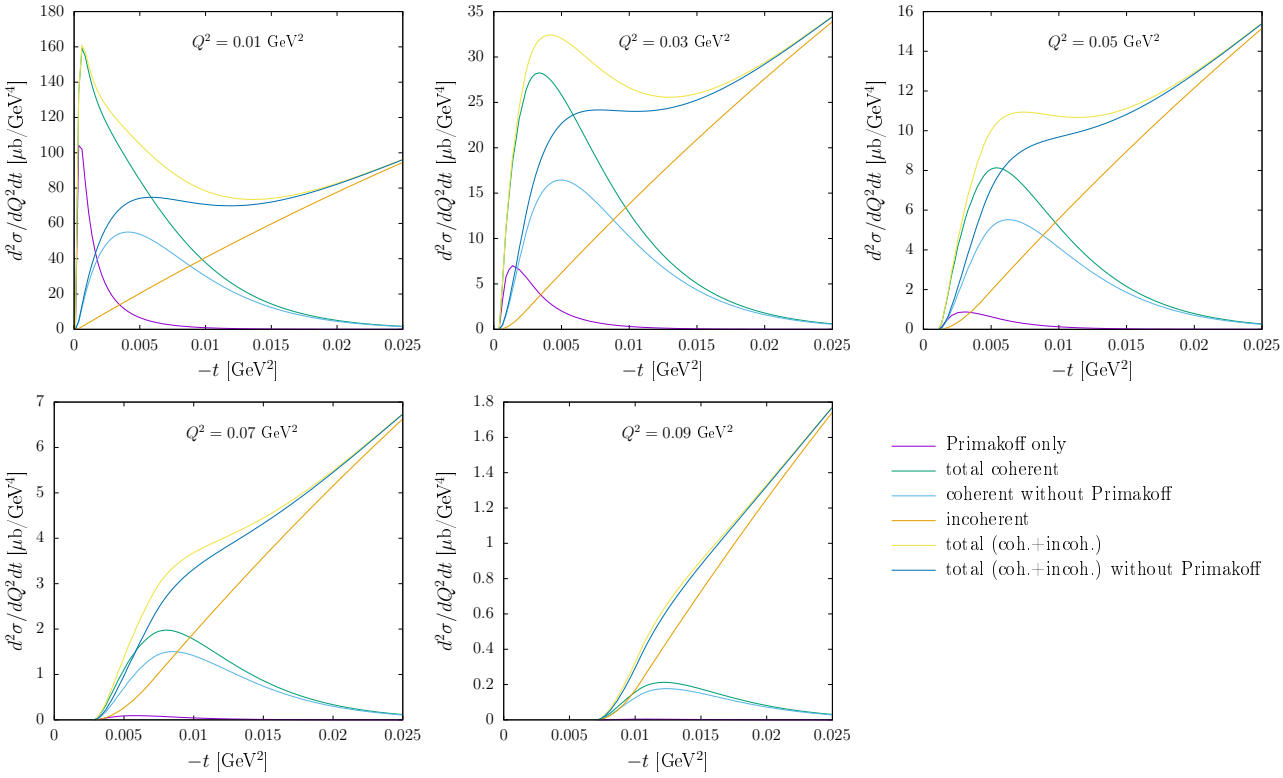

Figure 4: Differential cross sections $d^2\sigma/dQ^2dt$ as a function of t for different Q^2 values.

respect to the beam direction. This condition, combined with the fact that the pion energy is relatively high, implies that a large fraction of the γ particles emitted in the π^0 decay will also have momenta with relatively small angles to the beam direction, i.e. in the same range as the scattered electron momentum. In the following, a polar angle range from 5° to 15° for the detection of both electron and γs will be assumed. This will also become subject to optimisation studies, beyond the scope of this letter.

3.2 Cross section estimation

The expressions obtained in Section 2 are used to provide the estimates of the cross sections in Eqs. (15,18,19) in the kinematics of the proposed experiment, and to study the sensitivity of the observables to the Primakoff signal.

The nuclear electromagnetic form factor, entering the equations mentioned above, at small negative t can safely be approximated by the Gaussian $F_{Ch}(t) = \exp(R_{\rm ch}^2 t/6)$, where $R_{\rm ch} = 5.48$ fm [17] is the nuclear charge radius.[2]

The proton form factor is taken in the dipole form $G_E^p(t) = 1/(1 + |t|/\Lambda^2)^2$ with $\Lambda = 0.81$ GeV chosen to reproduce the proton charge radius ≈ 0.84 fm.

Results for this cross section as a function of t for several Q^2 values and separated among the various contributions discussed above are shown in Fig. 4. The sum of the

[2] ^{181}Ta is considered as target nucleus (see below).

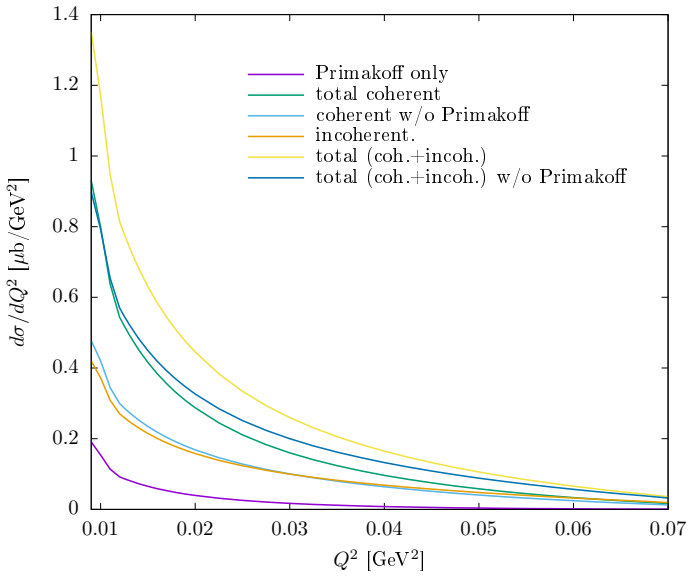

Figure 5: Single-differential cross sections $d\sigma/dQ^2$ as a function of Q^2.

coherent and incoherent production is shown in yellow, whereas the same sum under the assumption of no Primakoff contribution is shown in dark blue. The difference between these two curves offers the sensitivity to the pion TFF. The peak structure at low t, originating from the Primakoff production, is clearly visible at Q^2 values up to 0.05 GeV^2. For higher Q^2, the minimum accessible t value is too large and the Primakoff production becomes negligible.

Measurements at these largest values of Q^2 (and, consequently, t) can be used to fully determine the parameters of the background processes. Theoretical models will then be used to extrapolate this information down to the kinematics at which the Primakoff signal can be extracted.

The contribution coming from incoherent production is shown in orange and accounts for a significant portion of the overall distribution. A discrimination of this process by kinematical constraints would obviously enhance the sensitivity to the Primakoff contribution.

The total cross section decreases as a function of Q^2. The integral of $d^2\sigma/dQ^2dt$ over t from the lowest possible value up to $|t| = 0.015$ GeV^2 is shown in Fig. 5.

3.3 Pion acceptance correction

In order to detect and identify the π^0, and fully determine its momentum, both γ particles from its decay need to be detected. These are emitted isotropically in the pion rest frame, and their angular distribution in the laboratory frame is determined by the pion momentum. Knowing this distribution gives the possibility to calculate the fraction of events with a given pion momentum, in which both γs are emitted into the detector acceptance.

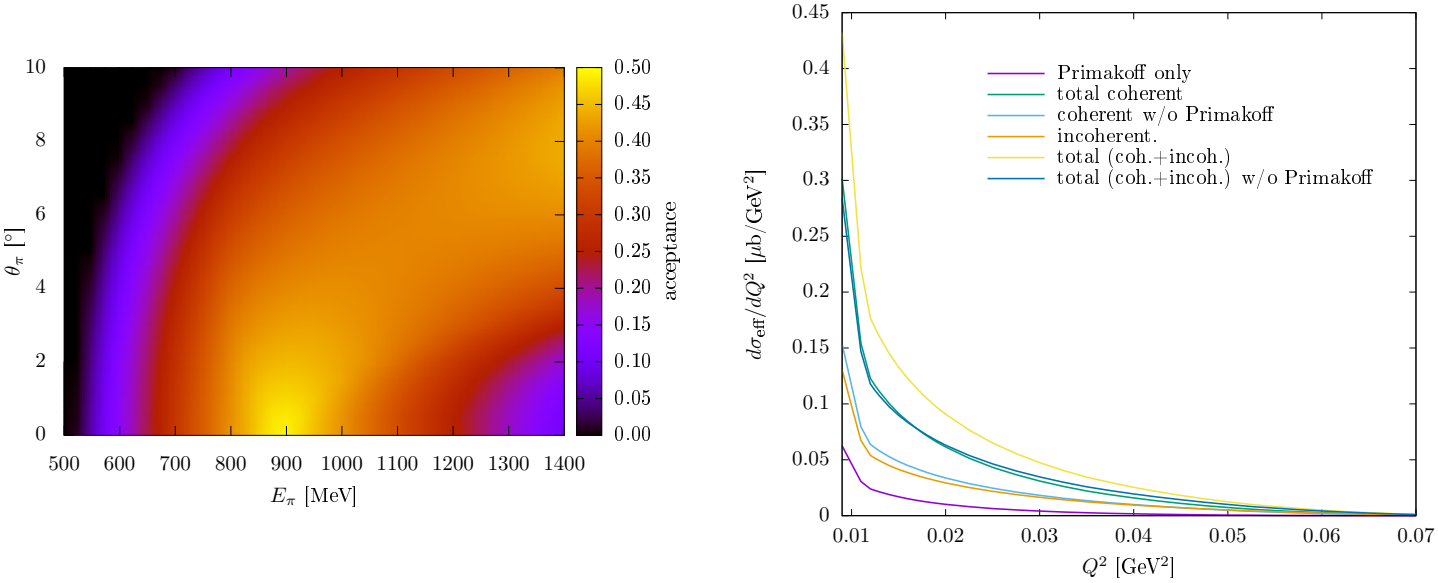

(a) (b)

Figure 6: (a) Pion detection probability as a function of the pion energy and emission angle with respect to the beam direction. The probability is calculated taking into account the angular acceptance for the decay γs, which are emitted isotropically in the pion rest frame. The detector efficiency is not taken into account. (b) Effective differential cross section $d\sigma_{\rm eff}/dQ^2$ as a function of Q^2, resulting from integrating the electroproduction cross section weighted with the pion detection probability over all other kinematical variables.

If one of the γ momenta has a direction given by the rest frame variables θ^* and φ^*, and the pion polar angle θ_π and energy ω_π in the laboratory frame are fixed, the polar angles $\theta_{1,2}$ of the γs in the laboratory frame can be calculated as $\theta_{1,2} = \theta_{1,2}(\theta^*, \varphi^*, \omega_\pi, \theta_\pi)$. Therefore an acceptance function $A(\omega_\pi, \theta_\pi)$ can be obtained as

$$A(\omega_\pi, \theta_\pi) = \frac{1}{2\pi} \int d\Omega^*_\gamma \Theta\left(\theta_1 - \theta_{\rm min}\right) \Theta\left(\theta_{\rm max} - \theta_1\right) \Theta\left(\theta_2 - \theta_{\rm min}\right) \Theta\left(\theta_{\rm max} - \theta_2\right) \ , \quad (21)$$

where $\Theta(x)$ is the Heaviside step function, and $\theta_{\rm min,max}$ define the polar angle acceptance range of the detector and are assumed to be equal to 5° and 15°, respectively. The resulting acceptance function is shown in Fig. 6-a. In the region of interest for the pion kinematics, the value of this function ranges between 10% and 50%. The edges of the acceptance are visible at high energy and small angles ($\theta_{\rm min}$), where one of the γs is always emitted into the inner hole of the detector, and at low energies ($\theta_{\rm max}$), where the opening angle between the γ momenta becomes large enough that at least one of the particles ends up always outside of the outer detector border.

Using the function in Eq. (21), effective cross sections can be calculated by weighting the fully differential cross sections with $A(\omega_\pi, \theta_\pi)$ when integrating over the kine-

matical variables, e.g.:

$$\frac{d^3\sigma_{\text{eff}}}{dE'd\Omega_e} = \int d\Omega_{\pi q}\; A\left(\omega_\pi, \theta_\pi\right) \frac{d^5\sigma}{dE'd\Omega_e d\Omega_{\pi q}}\,. \tag{22}$$

Similar weighted integral can be calculated to get $d^2\sigma_{\text{eff}}/dQ^2dt$ and $d\sigma_{\text{eff}}/dQ^2$. The latter is shown in Fig. 6-b. The comparison with Fig. 5 shows that the overall shape of the Q^2 dependence remains approximately the same but only about 20% to 30% of the events can be detected.

These estimations are also intended for assessing the rough feasibility of the experiment and are not meant to substitute Monte Carlo studies, including a detailed detector geometry description, as they are ongoing.

3.4 Proposed Setup

The measurement of the coherent π^0 electroproduction cross section can be performed at the A1 electron scattering facility, using the MAMI beam with an energy of 1.5 GeV [3] and a beam current up to 1 μA. As target, a tantalum ($Z = 73$) foil can be used.

The following upgrade of facility infrastructure in order to detect the scattered electron and the produced pion is proposed. Because the π^0 decays with almost 99% probability into two γs, it can be detected only using an electromagnetic calorimeter (EMC). Since the optimal kinematics for enhancing the Primakoff contribution results into electron scattering angles in the same range of the emission angles of the γs from the pion decay, also the electron needs to be detected with the same calorimeter. The detector needs to be placed at small forward angles and ideally cover the full azimuthal angle range, in order to maximise the acceptance. A ring-shaped calorimeter, installed downstream of the target around the exit beam pipe connecting the vacuum target chamber and the beam dump, is the ideal device (Fig. 7). The so-called EMP working group at the Helmholtz Institute Mainz, in collaboration with the Institute for Nuclear Physics of the Mainz University, is developing a part of the EMC for the future PANDA experiment at the upcoming FAIR facility in Darmstadt. Since the development of the detector is finished and the construction of the device has already started, it is eligible for taking part in the so-called phase 0 of FAIR, in which the use of FAIR equipment in other projects before the installation at FAIR is envisaged. The design of this detector matches the geometrical requirements for the experiment proposed in this letter, since it is intended to be placed at backward angles around the beam line inside the PANDA spectrometer. This calorimeter can be installed at A1, downstream of the target around the exit beam pipe.

In addition, a plastic scintillator detector has to be installed in front of the calorimeter, in order to distinguish between electrons and γ particles.

Spectrometer A of the A1 detector system will be needed as well and will play a crucial role for the alignment of the EMC.

[3] The optimal value of the beam energy needs to be determined but will lie in the range between 1.2 GeV and 1.5 GeV. In any case the use of MAMI-C is required.

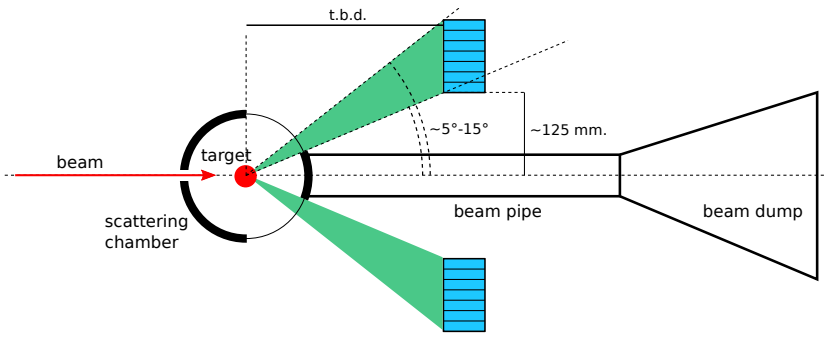

Figure 7: Schematic view of the foreseen experimental geometry. The calorimeter will be positioned downstream of the target around the beam pipe and will cover small scattering polar angles. The exact distance to the target and thus the angular coverage needs to be defined, based on optimisation studies.

In the following, more details about the setup for the proposed experiment are reported.

Target material

The nucleus which is intended to be used as target for the Primakoff measurement is ^{181}Ta. Tantalum has $Z = 73$ and presents the advantage of the very high melting temperature of over 3000°C. This allows for beam operation with high beam currents without need for a cooling system.

For calibration measurements, other targets will be needed during the experiment operation. In particular carbon, which is commonly used for the spectrometer calibrations, and plastics, which can be used as proton target for coincidence measurements.

The movable target system already available at A1 would perfectly match the needs of this experiment.

Electromagnetic calorimeter

A detailed description of the technological solutions used in the PANDA electromagnetic calorimeter can be found in ref. [26]. Here, the most salient features are recalled.

The active material of the calorimeter is the inorganic scintillator lead tungstate ($PbWO_4$), produced in the so-called PWO-II version. Its radiation length is 8.9 mm and its Molière radius 20 mm, allowing for a compact design of the detector. The decay time of the scintillation light is 6.5 ns and the light yield is 2.5% of NaI at -25°C, at which temperature the EMC is operated. The available crystals have a straight prism shape with the dimensions of $200\times24.5\times24.5$ mm^3. Their length corresponds to almost 22.5 radiation lengths, assuring a full longitudinal containment of electromagnetic showers. With the given transverse dimensions, 95% of the shower energy are typically deposited within a cluster of 9 crystals.

In total, 640 crystals are foreseen to be used in the A1 experiment. They will be arranged in 4×4 submodules (Fig. 8-a), which in turn will be supported from the back

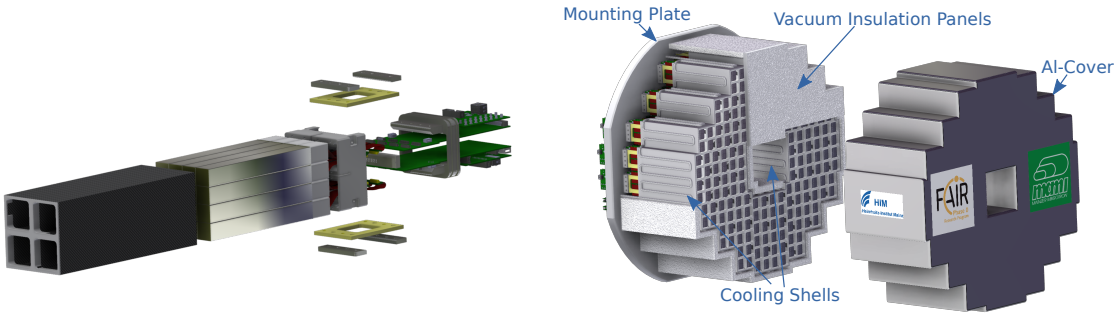

(a) (b)

Figure 8: (a) Exploded rendering of an EMC submodule with 16 PWO crystals (grey elements in the centre). The black part on the left is a crystal holding structure made of epoxy-reinforced carbon fibres. On the right, holding elements to fix the submodule to the mounting plate are visible, together with front-end electronics boards. (b) Rendering of the EMC layout foreseen for the A1 experiment.

by an aluminium mounting plate, in such a way that the crystals are parallel to the beam direction. The transverse area filled with crystals will be approximately ring-shaped with an inner diameter of 25 cm and an outer diameter of 75 cm. The polar angle coverage can be adjusted by changing the distance to the target. To fix the final value, the optimisation studies mentioned previously need to be completed. In Fig. 8-b a rendered picture of the detector is shown.

The scintillating light is detected with two large area avalanche photodiodes (APD) per crystal, with an active surface of 7×14 mm^2. Due to their large capacitance, a low-noise charge sensitive preamplifier is needed for their readout.

For this purpose, the "ASIC for the PANDA front-end electronics" (APFEL) has been developed by the GSI electronics department [27]. In the chip, the typical readout chain with charge preamplifier, shaper and main amplifier is implemented. One possible downside of this ASIC for the proposed experiment is the relatively long shaping time, of the order of some hundred nanoseconds, which is inconvenient for very high rate measurements. Although this is not an issue for PANDA, where the APFEL is not used in the very forward region, it will possibly be the limiting factor for the luminosity at the A1 experiment.

The APFEL signals are transmitted over 10 m long cables away from the detector area, and are digitised with sampling analogue to digital converters (SADC). The digitised signals are processed in FPGA units, in order to detect detector pulses and extract their energy and time information. SADC and FPGA units are installed on a digitiser board, developed for the PANDA Collaboration at the University of Uppsala.

This whole system has been tested and characterised with two prototypes, built after the design of a 16-crystal detector module. The prototypes were also tested with beam at the MAMI facility, both at A2 with tagged photons and with the electron beam at the X1 extraction line. In Fig. 9, a picture of one prototype together with

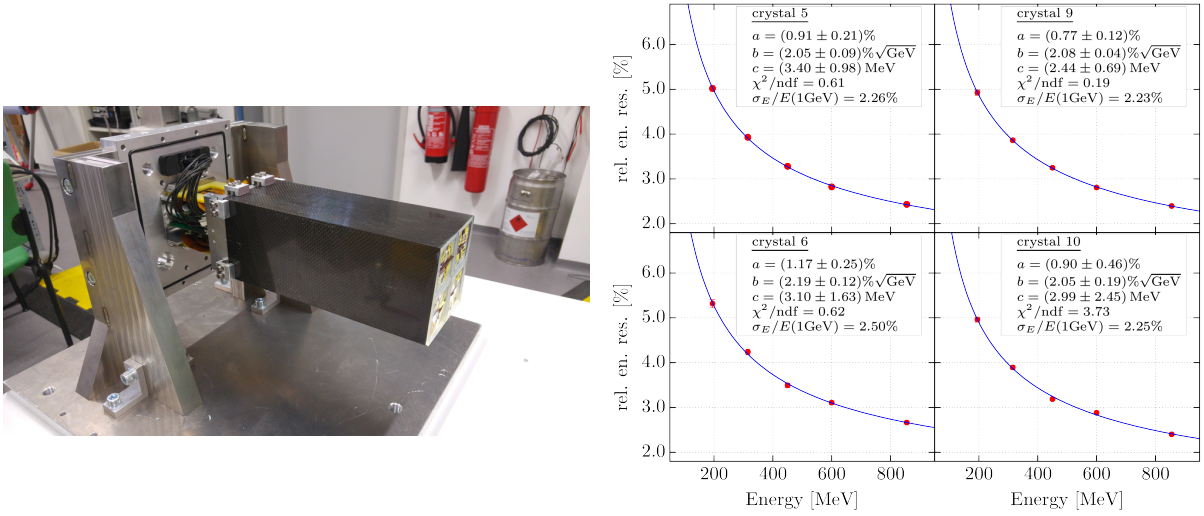

Figure 9: (a) Prototype calorimeter with 16 PWO crystals, built with the same design as a submodule of the final EMC. (b) Relative energy resolution, measured with the prototype EMC at the X1 test facility at MAMI, where the single crystals were centred one by one on the electron beam at various beam energies. The four plots correspond to the data with the four innermost crystals of the prototype in the beam. The energies were determined by summing the signals from a 3×3 crystal matrix. The fit function is of the usual form $(\sigma_E/E)^2 = a^2 + b^2/E + c^2/E^2$ [28].

results for the relative energy resolution is shown. The typical resolution is between 2.0% and 2.5% at a particle energy of 1 GeV. The position resolution was also studied, and values of the order of 1 mm were obtained. This translates at about 1 m distance to the target into an angular resolution of better than 0.1°.

Plastic scintillator detector

In order to reduce the combinatorial background of the measurement, the capability to distinguish between electrons and photons needs to be added to the detector system. To this end, a plastic scintillator system, placed in front of the calorimeter, is foreseen. A prototype of this detector has been built and operated in coincidence with the EMC prototype [29]. It is composed of two layers of four scintillator stripes each, with a thickness of 5 mm and a surface which matches the front face of a four-crystal row. From the coincidence between the two layers, a charged particle can be identified together with the crystal into which it is directed. This adds also some extra information about the particle momentum direction, which might become useful in the data analysis.

The scintillator stripes are read out with silicon photomultipliers. Their signals are then registered with the same front end electronics, which is already in use at the photon tagger in the A2 experiment. This system was developed by the electronics department of the Institute for Nuclear Physics in Mainz and has the advantage that, being already routinely in use at A2, is very well developed and tested. The same

readout system has already been used also at the A1 in another experiment.

The detailed geometry of the scintillator system needs yet to be designed.

Magnetic spectrometers

An accurate reconstruction of the momentum direction of the final state particles is crucial for the proposed experiment. If the t dependence of the differential cross section shown in Fig. 4 has to be resolved at the lowest Q^2 value, a resolution in t of the order of 10^{-4} GeV^2 is needed. The most significant impact on the determination of t comes from the transferred energy ν and from $\cos\theta_{\pi q}$. From Eq. (20), one derives that the ν resolution at the highest ν (lowest t) enters the t resolution with a weighting factor of about 10^{-2} GeV. Therefore, with an energy resolution at the percent level, the impact of the ν resolution on t is at the desired order of magnitude.

On the contrary, $\cos\theta_{\pi q}$ is weighted with a large factor of up to 4 GeV^2, setting a required resolution of about 0.4° for $\theta_{\pi q}$, which is in turn a combination of three different, directly measured angles. These should be thus measured with a resolution of roughly 0.2°. The angular resolution is given by the resolution of the position measurement with the EMC and the accuracy on the position of the calorimeter itself with respect to the target and the beam. Both of these accuracies need to be at the millimetre level in order to guarantee the needed angular resolution. Supposing that this is the case for the position measurement with the EMC, a procedure is required for determining the detector position with the same accuracy. It should be noted, that the relevant information is not quite the calorimeter position with respect to the hall, which should be easily determined at the millimetre level or better, but rather the position of the beam spot on the target and the beam direction with respect to the EMC. These parameters might vary significantly among different data taking runs, since the beam position and direction change after every beam optimisation. For this reason, a beam position measurement with one of the magnetic spectrometers of the A1 facility is needed periodically as position reference. Submillimetre statistical accuracies can be obtained within few minutes with the available apparatus. The relative position of spectrometer and EMC can then be obtained by measuring a known scattering process like elastic scattering on hydrogen (doable with a plastic target) with the spectrometer detecting the recoil proton and the calorimeter the electron in coincidence.

The magnetic spectrometers will play an important role also for the energy calibration of the EMC. Also in this case, a coincidence readout of both detector systems is needed. Among others, the best candidate for the energy calibration is probably the single π^0 production on the proton. For this purpose, the electron can be detected with a spectrometer, which would fix the dependence of the π^0 momentum on its emission angle. The decay γs would then be emitted over the full calorimeter surface, allowing for energy calibration through a global fit on the detected event sample. An improvement of the accuracy of this method would come from measuring the same process in triple coincidence, where a second spectrometer detects the recoil proton. This procedure would add a very useful redundancy, but its feasibility in terms of statistical accuracy might be an issue and should be investigated.

Data readout
For collecting the hit information from all detector modules, the so-called TRB system, developed at the GSI for the Hades and CBM collaborations, was chosen. This system has the advantage that all needed functionalities are already implemented and it is maintained and further developed by a larger community. Moreover, it has already been interfaced to the A1 readout electronics for another experiment.

In order to perform coincidence measurements with the EMC and the magnetic spectrometers, a common trigger signal is needed for starting the readout of both systems. In the original EMC readout, the signals are continuously digitised and the pulse detection happens after digitisation, introducing large latencies of the order of many microseconds. The spectrometer signals instead are digitised only if a trigger signal is present. The EMC electronics latency is therefore too long for building a coincidence. For this reason, an extra analogue circuit will be introduced before the input to the SADC boards, in order to discriminate the signals before digitisation. For each submodule, the signals of all 16 crystals will be summed and fed into a constant fraction discriminator (CFD). A logical OR of the outputs of all CFD will be generated and sent to the spectrometer electronics for obtaining the coincidence trigger signal. This will be sent back to the EMC electronics for starting the data acquisition, together with a unique event number. The data of the two systems will be read out independently into two separated data streams. Eventually, the event information can be recombined offline, based on the event number. This system has worked already successfully in a test experiment, as described below.

Hall integration
In order to operate the calorimeter in the A1 hall, no extra infrastructure is needed than what is already available. The full EMC needs essentially the same services as the prototype calorimeter, which was already operated in the A1 hall.

- For cooling the detector, a refrigerating unit will be used, which needs a dedicated line of cooling water for the operation. One of the available cooling water lines will be needed.

- When the detector is at the operating temperature of $-25°$C, its inner volume is flooded with nitrogen in order to prevent ice formation. One of the available gas lines from the detector laboratory to the hall will be needed.

- For the readout and control of the calorimeter, some electronic equipment will be needed, which is expected to fit in one rack. Some space in one of the radiation shielded areas will be sufficient.

- The space for cable routing from the detector position to the rack will have to be freed.

The only major modification in the hall setup concerns the target area. The available vacuum chambers for the target do not have a sufficiently wide window in the forward scattering region. Therefore, a new chamber is being designed, in order to

have a free particle path from the target to the calorimeter and to the spectrometers over the whole acceptance range.

The usual layout of the A1 vacuum chambers features a vertical cylindrical body, where the beam pipe is attached, and an upper and lower cap, through which the target services are fed into the vacuum volume. Only the cylindrical part will be manufactured anew, while keeping the same dimensions of the older chambers. This way, the full A1 target system can be operated without any further modification.

Depending on the final position of the calorimeter along the beam axis, it might happen, that also the exit beam pipe, connecting target chamber and beam dump, needs to be redesigned.

Selection of electroproduction events

By triggering the readout of the digitised signals when a sufficient amount of energy has been measured over the whole calorimeter, a very high detection efficiency for the scattering events of interest is obtainable. Inevitably, other scattering processes will also generate detector events. In order to count the number of π^0 electroproduction events and determine the cross section, the recorded events originating from this process need to be selected in an offline analysis.

The signature of the reaction would be given therefore by the following requirements:

1. three energy clusters are detected in the calorimeter,
2. the energy sum of all three clusters is close to the beam energy,
3. one cluster corresponds to a charged particle, while the other two to neutral particles, and
4. the two clusters corresponding to neutral particles have an invariant mass in the vicinity of the pion mass m_π.

These constraints need to be optimised with simulations and with the real data itself. For instance, condition 3. might need to be mitigated to account for events where a γ particle converts before or inside the plastic scintillator detector and is wrongly identified as charged particle.

4 Feasibility Studies

Two detector tests with beam were performed at the A1 facility during 2018. The aim of the tests was to prove the technical viability of the proposed experiment. Here, their outcome is briefly summarised, whereas more detailed information can be found in [30].

Since the measurement of the electroproduction cross section in the Primakoff kinematical regime requires the detection of particles at very small forward scattering angles, where high particle fluxes are expected, one first question to assess is whether the detector system can be operated at such high rate of incoming particles.

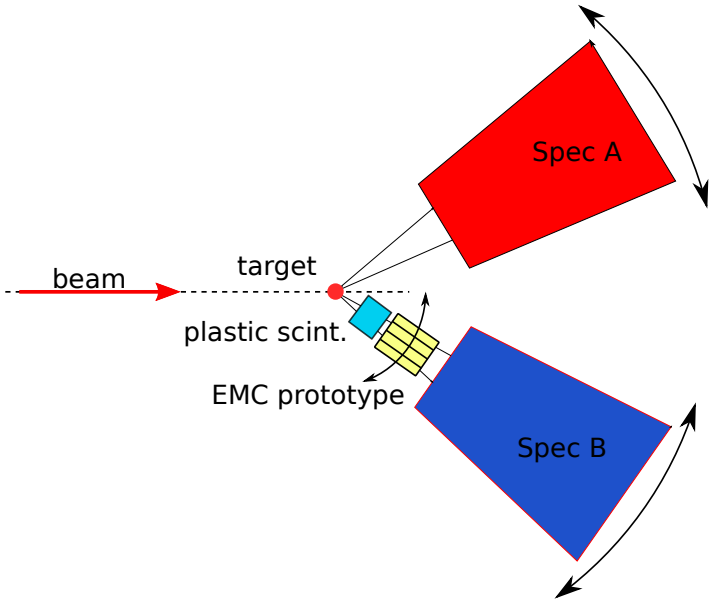

(a)

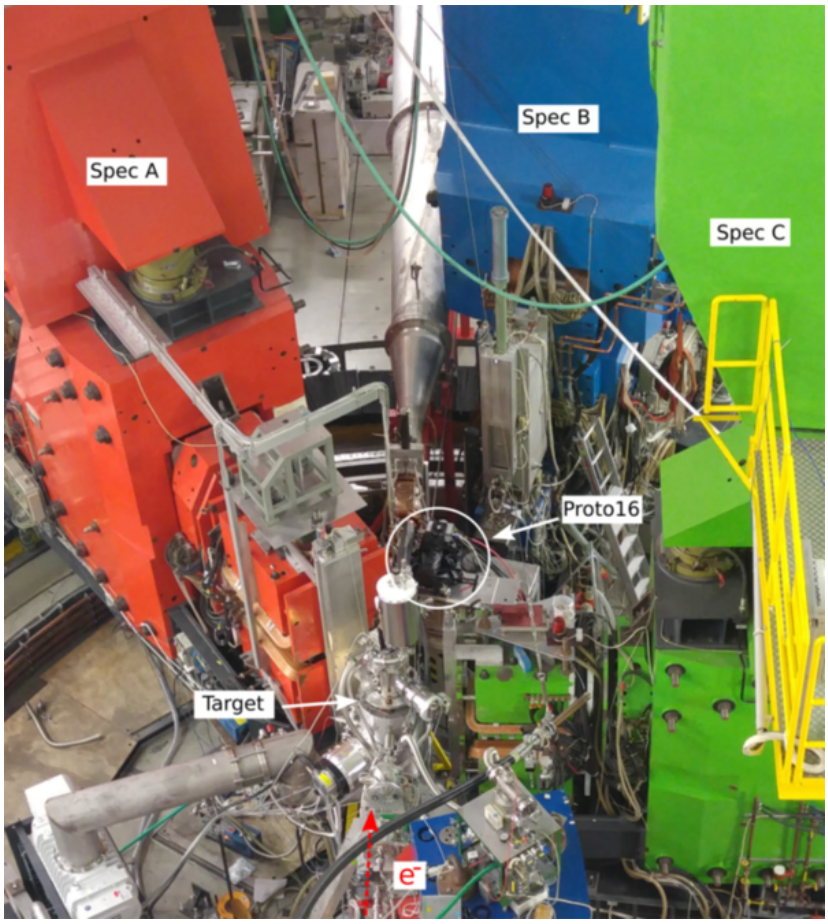

(b)

Figure 10: (a) Sketch of the beam test setup with the protoype EMC at the A1. See explanation in the text. (b) Picture of the setup.

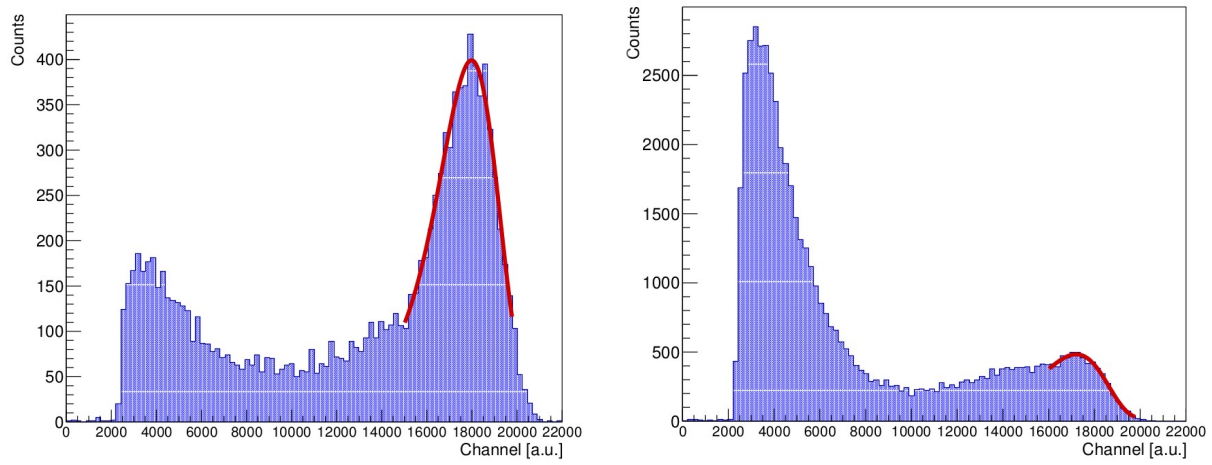

(a) (b)

Figure 11: Energy spectra recorded with the prototype calorimeter at the A1 with a beam energy of 1.5 GeV and at the scattering angle of 8.5°. The targets were carbon (a) and ^{181}Ta (b). The unit in the abscissa is given by the pulse height extraction algorithm in use and is proportional to the sum of the energies measured in a 3×3 crystal matrix. The peak structures on the left correspond to the quasi-elastic scattering off single nucleons in the target and is fit with the phenomenological Novosibirsk function [30]. The events at low energies are predominantly γ particles from neutral pion decays.

To this end, the EMC prototype described above was installed and brought into operation in the A1 hall (Fig. 10). It was installed on the movable platform of spectrometer B, where usually the inlet vacuum chamber between the target vessel and the entrance of the first spectrometer magnet is located. Instead of the vacuum chamber, a support table was mounted in order to position the EMC prototype at the beam height. The advantage of this configuration was that the prototype had to be aligned only with respect to the spectrometer B, whose position with respect to the target and the beam is very well known. In addition, it was possible to change the scattering angle covered by the prototype, by rotating the spectrometer, which is also a very well established operation at A1. The distance between the interaction point and the EMC front surface was 128 cm and the total angular coverage in the polar angle θ was 4.5°. Measurement at various central angles ranging from the minimum of 8.7° up to 25° were performed, using three different targets: ^{12}C, ^{181}Ta and plastics.

At the smallest angles, the prototype covered a θ range from 6.5° to 10.9°, which is in the same range where the detector for the Primakoff measurement should be positioned. At these angles, it was possible to record energy spectra where the contributions from the expected physics processes are clearly visible. Two examples are given in Fig. 11. On the upper end of the spectrum the peak of corresponding to the quasi-elastic scattering on the nucleons inside the target nucleus is visible both for carbon and tantalum. The widths of the quasi-elastic peaks are roughly within the expectations based on the detector resolution and the spread coming from the Fermi

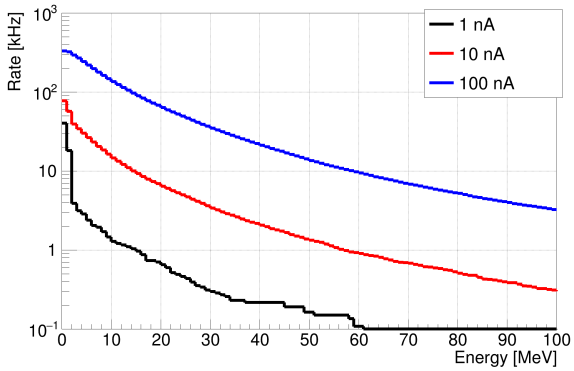

Figure 12: Measured detector rates in a single crystal at low energies for different values of the beam current. The polar scattering angle is about 7°. The bin content represents the total rate of pulses with an energy larger than the bin position. The structure at very small energies is the electronics noise, whose rate is independent of the beam current. It is dominant at 1 nA while negligible at 100 nA.

momentum of the nucleon. On the low energy end, the spectrum is expected to be dominated by the γ particles from the π^0 decay.

Once it has been proven that the calorimeter operation is possible under the given conditions, a second question to be addressed concerns the maximum luminosity which the detector can cope with. When the beam current is increased, the total flux of particles getting into the detector increases, with low energy particles having the highest rates. Since the preamplifier pulses have a relatively long rise time of about 300 ns, the pile-up probability of signal pulses becomes significant already at moderate rates of some hundred kilohertz. If the pulses to be measured are likely overlapped with other low energy pulses, the pulse height extraction is randomly biased and an effective deterioration of the energy resolution occurs. In order to estimate the extent of this effect, single channel (crystal) rate measurements in the low energy region have been performed with different beam currents and at the smallest possible scattering angles. The results are shown in Fig. 12 for 1 nA, 10 nA and 100 nA, respectively. The measured rates scale very well with the beam current, which is a first evidence that with these currents the detector has not yet reached saturation due to the dead-time. Taking into account density and thickness of the Ta target in use, one has a luminosity of 5.55 $(\mu\mathrm{b})^{-1}/s$ at 100 nA. At least with this luminosity, a measurement appears feasible. In the meantime, a detailed simulation of the overlap of signal pulses based on the rate measurements presented here is ongoing [31], in order to estimate the effect of the pile-up on the energy resolution, and possibly find a higher value of the luminosity which is still viable.

A third technical aspect which has proven feasible through the beam tests is the detection of physics events in coincidence between the calorimeter and a magnetic spectrometer. The trigger and readout system described above were implemented and brought into operation.

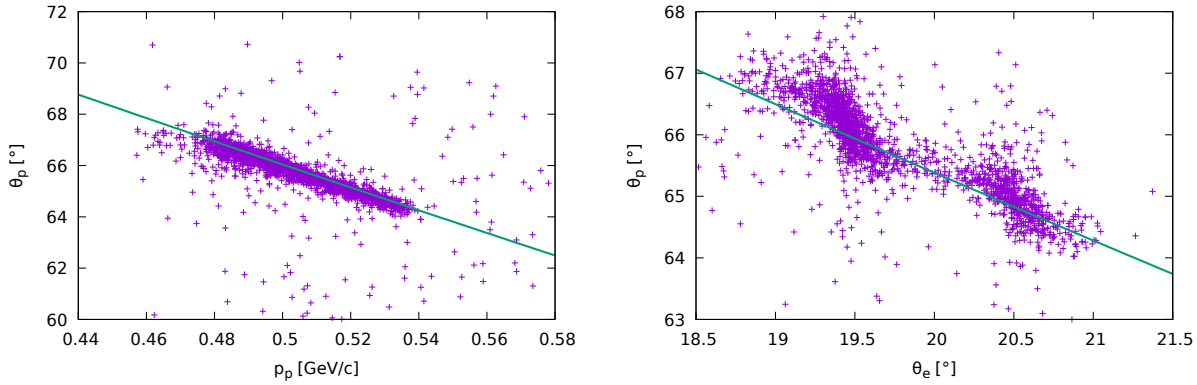

(a) (b)

Figure 13: Data recorded with the EMC prototype and spectrometer A triggered in coincidence. The central polar angles of the two detectors where chosen in order to select elastic electron proton scattering events. The electron was detected with the calorimeter and the proton with the spectrometer. The correlation between the proton angle θ_p and momentum p_p, measured with the spectrometer are shown in (a) together with the expected kinematical curve (in green). The ranges of the θ_p and p_p distributions are determined by the calorimeter acceptance. (b) shows the correlation between θ_p and the electron scattering angle θ_e reconstructed with the EMC data. The curve shows again the expectation from kinematics.

The elastic electron proton scattering was chosen as scattering process to be detected, because the kinematics has only one free parameter, e.g. the polar scattering angle of the electron θ_e, since the A1 spectrometer can detect particles on the accelerator plane (i.e. the azimuthal scattering angle can not be varied). If this variable is selected, all other variables, i.e. the electron energy and the recoil momentum and angle of the proton, are fixed. The prototype EMC was positioned at three different angles for detecting the electron, while spectrometer A was moved to the corresponding proton angles.

A polyurethane (plastics) target was used, because it contains hydrogen atoms. The quasi-elastic scattering off the carbon nuclei inside the target material is the only significant background, although the detected events are dominated by the proton scattering.

In Fig. 13, selected results of these measurements for $\theta_e = 20°$ are shown. On the right, the proton variables measured with the spectrometer are shown. On the left, the proton recoil angle θ_p is plotted against θ_e, reconstructed from the calorimeter data using a linear weighting ansatz for calculating the impact position (x, y) from the energies E_i measured in the crystals:

$$(x, y) = \sum_{i=0}^{15} E_i \cdot (x_i, y_i) \ , \tag{23}$$

Q_0^2 [GeV^2]	σ [nb]	$\sigma_{\rm eff}$ [nb]	$T(1\%)$ [h]	$N(1000{\rm h})$	$d\sigma_{\rm eff}^{\rm stat}/\sigma_{\rm eff}$ [%]
0.01	10.076	2.951	170	58967	0.41
0.02	4.579	0.936	535	18708	0.73
0.03	2.635	0.483	1035	9658	1.02
0.04	1.664	0.257	1944	5143	1.39
0.05	1.068	0.127	3938	2539	1.98
0.06	0.662	0.051	9719	1028	3.12

Table 1: Total cross sections and effective cross sections for various Q^2 bins are given in columns 2 and 3. The bin width is 0.01 GeV^2 and the bin centres are given in the column 1. Column 4 gives the needed measuring time for obtaining a 1% statistical uncertainty in the cross section measurement, while the number of events obtainable with 1000 hours of measuring times along with the corresponding statistical uncertainty are given in columns 5 and 6, respectively.

where (x_i, y_i) are the positions of the crystals on the transverse plane.

From Fig. 13-b, the correlation between θ_p and θ_e is clearly visible, proving that, for each point, spectrometer and EMC data correspond to the same event. Moreover, the data lie with some approximation on the curve expected from kinematics. Obviously, the position reconstruction in the EMC needs to be improved. For instance, Eq. (23) assumes a linear behaviour for the lateral electromagnetic shower profile, which is a very rough approximation and results into a bias of the data points towards the centre of the crystals, explaining the two-cluster structure of the distribution. Also the relative calibration of the crystal signals could be improved, and might be the explanation of the wrong slope of the two single clusters. In order to optimise these aspects, detailed simulations are ongoing and probably more beam tests will be needed.

5 Beam Time Estimation

In order to estimate the experiment running time, needed for the measurement of the electroproduction cross section, the effective differential cross section $d\sigma_{\rm eff}/dQ^2$ shown in Fig. 6-b, which takes into account the pion detection probability, has been integrated over 6 Q^2 bins with a width of 0.01 GeV^2 for central values from 0.01 GeV^2 to 0.06 GeV^2. The interval of integration over t ranges from 0 to 0.015 GeV^2. The assumed luminosity is, like quoted above, 5.55 $(\mu{\rm b})^{-1}/s$, corresponding to a beam current of 100 nA. The results are presented in Table 1. The second and third columns give the total and the effective cross sections. In the fourth column, the number of hours needed for a 1% relative statistical uncertainty (10000 events) are shown. The last two columns contain the number of events and the corresponding statistical uncertainty for a running time of 1000 h, which is assumed as the maximum reasonable beam time for this experiment.

Measurements for the low Q^2 region up to 0.03 GeV^2 are feasible at the percent level within 1000 h or less. For the higher Q^2 values, only larger uncertainties are

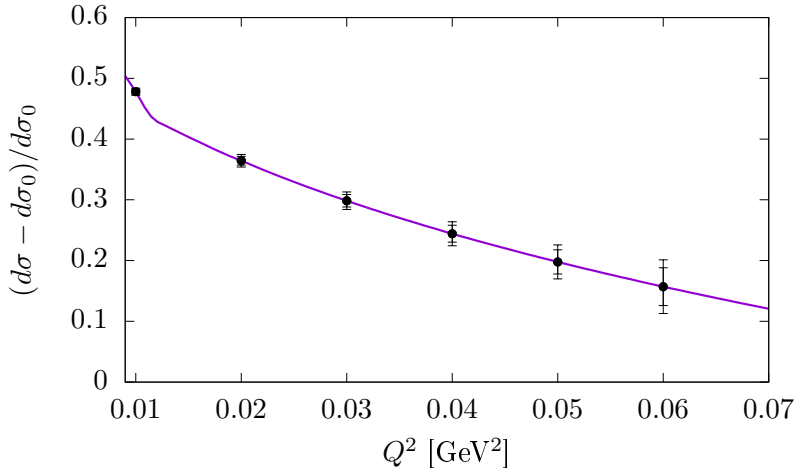

Figure 14: Difference between the expected cross section with and without Primakoff contribution, normalised to the latter one, as a function of Q^2. The points show the possible measurements and the error bars indicate the expected statistical uncertainties for 1000 and 500 hours of measuring time, respectively.

attainable.

The strongest sensitivity to the Primakoff contribution and thus to the pion TFF is present at low Q^2. In Fig. 14, the quantity

$$\left(\frac{d\sigma}{dQ^2} - \frac{d\sigma_0}{dQ^2}\right) / \frac{d\sigma_0}{dQ^2} \ , \tag{24}$$

where σ_0 stands for the cross section without the Primakoff contribution, is shown. The points represent the possible measurements and the error bars correspond to 1000 h and 500 h of data taking, respectively.

Since the pion TFF multiplies the Primakoff contribution to the scattering amplitude, this plot shows to some extent the sensitivity of the cross section measurement to the form factor. In order to actually extract the form factor for each Q^2 value, a fit to the t dependence shown in Fig. 4, with an appropriate model for the background needs to be performed. The measurements at higher t values, which happen simultaneously and are not sensitive to the Primakoff reaction, will be very important for constraining the parameters of the background model, thus mitigating the model dependence. The systematic uncertainty associated with this model dependence needs yet to be assessed, and reported in a full proposal for the experiment.

Given the numbers in Table 1, a two stages experiment is foreseeable, where a preliminary run of around 100 hours to prove the feasibility at low Q^2 is performed, on the basis of which, a decision for a longer run to cover the higher Q^2 range can be made.

The most important requirements for the experiment are summarised in Table 2.

Beam	energy	1.2 to 1.5 GeV
	current	0.1 to 1.0 μA
	polarisation	unpolarised
Target material		^{181}Ta
Detector systems		EMC (new) plastic scintillator (new) A1 spectrometer A
Beam time for	tests	24 h
	pilot experiment	100 h
	full experiment	1000 h

Table 2: Summary of the experiment requirements.

References

[1] T. Blum, A. Denig, I. Logashenko, E. de Rafael, B. L. Roberts, T. Teubner and G. Venanzoni, arXiv:1311.2198 [hep-ph].

[2] K. Hagiwara, R. Liao, A. D. Martin, D. Nomura and T. Teubner, J. Phys. G **38** (2011) 085003 doi:10.1088/0954-3899/38/8/085003 [arXiv:1105.3149 [hep-ph]].

[3] G. W. Bennett *et al.* [Muon g-2 Collaboration], Phys. Rev. D **73** (2006) 072003 doi:10.1103/PhysRevD.73.072003 [hep-ex/0602035].

[4] J. L. Holzbauer [Muon g-2 Collaboration], PoS NuFact **2017** (2018) 116 doi:10.22323/1.295.0116 [arXiv:1712.05980 [hep-ex]].

[5] T. Aoyama, M. Hayakawa, T. Kinoshita and M. Nio, Phys. Rev. Lett. **109** (2012) 111808 doi:10.1103/PhysRevLett.109.111808 [arXiv:1205.5370 [hep-ph]].

[6] C. Gnendiger, D. Stckinger and H. Stckinger-Kim, Phys. Rev. D **88** (2013) 053005 doi:10.1103/PhysRevD.88.053005 [arXiv:1306.5546 [hep-ph]].

[7] J. Prades, E. de Rafael and A. Vainshtein, Adv. Ser. Direct. High Energy Phys. **20** (2009) 303 doi:10.1142/9789814271844.0009 [arXiv:0901.0306 [hep-ph]].

[8] G. Colangelo, M. Hoferichter, B. Kubis, M. Procura and P. Stoffer, Phys. Lett. B **738** (2014) 6 doi:10.1016/j.physletb.2014.09.021 [arXiv:1408.2517 [hep-ph]].

[9] V. Pauk and M. Vanderhaeghen, Phys. Rev. D **90** (2014) no.11, 113012 doi:10.1103/PhysRevD.90.113012 [arXiv:1409.0819 [hep-ph]].

[10] G. Colangelo, M. Hoferichter, M. Procura and P. Stoffer, JHEP **1509** (2015) 074 doi:10.1007/JHEP09(2015)074 [arXiv:1506.01386 [hep-ph]].

[11] M. Hayakawa and T. Kinoshita, Phys. Rev. D **57** (1998) 465 Erratum: [Phys. Rev. D **66** (2002) 019902] doi:10.1103/PhysRevD.57.465, 10.1103/PhysRevD.66.019902 [hep-ph/9708227].

[12] K. Melnikov and A. Vainshtein, Phys. Rev. D **70** (2004) 113006 doi:10.1103/PhysRevD.70.113006 [hep-ph/0312226].

[13] P. Masjuan and P. Sanchez-Puertas, Phys. Rev. D **95** (2017) no.5, 054026 doi:10.1103/PhysRevD.95.054026 [arXiv:1701.05829 [hep-ph]].

[14] I. Larin *et al.* [PrimEx Collaboration], Phys. Rev. Lett. **106** (2011) 162303 doi:10.1103/PhysRevLett.106.162303 [arXiv:1009.1681 [nucl-ex]].

[15] B. L. Ioffe and A. G. Oganesian, Phys. Lett. B **647** (2007) 389 doi:10.1016/j.physletb.2007.02.021 [hep-ph/0701077].

[16] H. Primakoff, Phys. Rev. **81** (1951) 899. doi:10.1103/PhysRev.81.899

[17] C. W. De Jager, H. De Vries and C. De Vries, Atom. Data Nucl. Data Tabl. **14** (1974) 479 Erratum: [Atom. Data Nucl. Data Tabl. **16** (1975) 580]. H. De Vries, C. W. De Jager and C. De Vries, Atom. Data Nucl. Data Tabl. **36** (1987) 495. doi:10.1016/S0092-640X(74)80002-1

[18] G. Faeldt, Nucl. Phys. B **43** (1972) 591. doi:10.1016/0550-3213(72)90039-9

[19] S. Gevorkyan, A. Gasparian, L. Gan, I. Larin and M. Khandaker, Phys. Rev. C **80** (2009) 055201 doi:10.1103/PhysRevC.80.055201 [arXiv:0903.4715 [hep-ph]].

[20] M. Gorchtein, P. Guo and A. P. Szczepaniak, Phys. Rev. C **86** (2012) 015205 doi:10.1103/PhysRevC.86.015205 [arXiv:1102.5558 [nucl-th]].

[21] T. H. Bauer, R. D. Spital, D. R. Yennie and F. M. Pipkin, Rev. Mod. Phys. **50** (1978) 261 Erratum: [Rev. Mod. Phys. **51** (1979) 407]. doi:10.1103/RevModPhys.50.261

[22] S. Gevorkyan, A. Gasparian, L. Gan, I. Larin and M. Khandaker, Phys. Part. Nucl. Lett. **9** (2012) 3 doi:10.1134/S1547477112010116 [arXiv:0908.1297 [hep-ph]].

[23] D. N. Goswami, D. P. Majumdar, Phys. Rev. D **8**, 2086 (1973)

[24] M. Tanabashi et al. (Particle Data Group), Phys. Rev. D **98**, 030001 (2018)

[25] M. Gorshteyn, private communication

[26] W. Erni *et al.* [PANDA Collaboration], arXiv:0810.1216 [physics.ins-det]

[27] P. Wieczorek, H. Flemming, IEEE Nucl.Sci.Symp.Conf.Rec. 2010, 1319-1322

[28] U. Amaldi, Physica Scripta, Vol. **23** (1981), 409-424

[29] P. Grasemann, Master Thesis, University of Mainz, 2018

[30] S. Wolff, Master Thesis, University of Mainz, 2018

[31] O. Noll, PhD Thesis in Preparation, University of Mainz